Surface & Coatings Technology 481 (2024) 130615

Contents lists available at ScienceDirect

Surface & Coatings Technology

journal homepage: www.elsevier.com/locate/surfcoat

Full Length Article

Preparation and cavitation erosion resistance of nanocrystalline surface layer on 304 stainless steels

Nengliang Huang [a,b,1], Ye Tian [b,1], Rui Yang [b,1], Honghai Ma [c], Xiuyong Chen [a,*], Xinkun Suo [a,*], Hua Li [b,*]

[a] Faculty of Mechanical Engineering & Mechanics, Ningbo University, Ningbo, Zhejiang 315211, China
[b] Zhejiang-Japan Joint Laboratory for Antibacterial and Antifouling Technology, Zhejiang Engineering Research Center for Biomedical Materials, Cixi Institute of Biomedical Engineering, Ningbo Institute of Materials Technology and Engineering, Chinese Academy of Sciences, Ningbo 315201, China
[c] Kwh (Hangzhou) Technology Co., Ltd., Hangzhou 311215, China

ARTICLE INFO

Keywords:
304 stainless steels
Cavitation erosion
Martensite
Nanocrystalline layer

ABSTRACT

Cavitation erosion is a common damage form of hydraulic components. Constructing a cavitation-erosion-resistant layer on the surface of hydrodynamic components can effectively prolong the service life of the equipment. In this study, 304 austenitic stainless steel was machined by a diamond blade under specific processing parameters, and a nanocrystalline layer (304-Nano) was formed by the work hardening during the machining process. The machining process also allowed strain-induced martensitic transformation, creating martensite in the nanocrystalline layer. The nanocrystalline layer had an average grain size of approximately 34.7 nm, showing a Vickers hardness of 600 ± 30 Hv, which was much higher than that of the original 304 austenitic stainless steel (230 ± 14 Hv). After the 15-h cavitation erosion test, the cavitation erosion rate of the 304-Nano sample was only 19.4 % that of the original ordinary 304 stainless steel, showing that the 304-Nano sample has excellent cavitation erosion resistance. Furthermore, the in-situ SEM results showed that the 304-Nano sample could significantly inhibit crack propagation, which was probably attributed to its high density of grain boundaries and ultrahigh hardness. The excellent cavitation erosion resistance of the nanocrystalline layer is expected to be used as a protective material for anti-cavitation erosion applications.

1. Introduction

During the operation of hydraulic components, a high-velocity fluid can create a low-pressure zone on the component surface and cause the formation of vapour-filled bubbles, which are cavitation bubbles [1,2]. The implosion of some cavitation bubbles can apply repeated impacts, whose pressure can range from several MPa to 10^3 MPa or even 10 GPa according to experiments and numerical studies [3–5], to the component surface nearby, causing plastic deformation and rupture of the material. The wear caused by cavitation is termed cavitation erosion, which is a common failure mode of hydrodynamic components such as propellers, impellers, pumps, and valves [6–8]. Since cavitation erosion damages the surface of materials, applying protective coatings is a common and feasible method to protect hydraulic components against cavitation erosion. Recent studies have reported that coatings with nanocrystalline structures possess good cavitation erosion resistance. Hong et al. deposited near-nanostructured WC-10Co4Cr coatings onto 1Cr18Ni9Ti stainless steel using high-velocity oxygen-fuel (HVOF) spraying, and the erosion of the former was 78 % that of the latter after the exposure to cavitation for 10 h [9]. Qiao et al. prepared an HVOF-sprayed Fe-based amorphous/nanocrystalline coating, whose erosion was only 1/6 that of A321 stainless steel [10]. Other studies also showed that the coatings with nanocrystalline structure exhibited good cavitation erosion resistance [11–14]. Additionally, it is worth mentioning that the cavitation erosion resistance of the coatings is material-dependent. For example, Nowakowska et al. showed that nano Al_2O_3-TiO_2 coating did not grant enhancement in cavitation erosion resistance [15].

Apart from the deposition of coatings, the surface engineering techniques without introducing other materials can effectively improve the cavitation erosion resistance. For example, friction-stir processing (FSP) could refine the grains in a material by plastic deformation and

* Corresponding authors.
E-mail addresses: chenxiuyong@nbu.edu.cn (X. Chen), suoxinkun@nbu.edu.cn (X. Suo), lihua@nimte.ac.cn (H. Li).
[1] These authors contributed equally to this work.

https://doi.org/10.1016/j.surfcoat.2024.130615
Received 30 November 2023; Received in revised form 31 January 2024; Accepted 29 February 2024
Available online 8 March 2024

Table 1
Chemical composition of the AISI 304 stainless steel (according to the specification from the supplier).

Elements	C	Cr	Ni	Mn	Si	P	S	Fe
wt%	0.08	18	8.01	1.95	1.00	0.033	0.028	Bal.

enhance cavitation erosion resistance [16–19]. Selvam et al. refined the surface of 316 L stainless steel to an average grain size of about 600 nm by FSP, and the FSP stainless steel exhibited cavitation erosion resistance that was about 4–6 times that of the original 316 L stainless steel [16]. Escobar et al. refined the grain size of S32205 duplex stainless steel from about 6 μm to about 1–3 μm and enhanced cavitation erosion resistance [17]. However, there are very few studies on the cavitation erosion resistance of the material whose microstructure is refined by strain-induced methods other than FSP. Meanwhile, nanocrystalline materials (grain size less than 100 nm) have outstanding mechanical properties [20], which are beneficial to resisting cavitation erosion. Nevertheless, the materials treated by FSP usually cannot achieve such a refined microstructure, but mechanical grinding may introduce a nanocrystalline layer to the ground material [21].

This work aims to refine the microstructure of the 304 stainless steel via a machining process. The microstructure, mechanical properties, and cavitation erosion resistance of the processed 304 stainless steel were investigated, and the failure mechanism of the materials exposed to cavitation erosion in deionized water was further explored.

2. Materials and methods

2.1. Sample preparation

This work used a bar of AISI 304 stainless steel whose diameter was 20 mm. The chemical composition of the stainless steel was tabulated in Table 1. The stainless steel bar was cut into cylinders with a thickness of 10 mm in a cutting machine (Brillant, ATM, Germany), and a diamond blade (Dongguan Kechuang Grinding Materials Ltd., China) with a diameter of 125 mm was used. During the cutting, the rotation speed of the blade was 3800 rpm, the feed rate was 0.04 mm/s, and the blade was continuously hosed down with tap water. Then, a group of the stainless steel cylinders were ground on 240-, 400-, 800-, 1200-, and 2000-grit SiC paper and polished by 50 nm SiO_2 suspension, which were denoted as the 304 samples. The other group of the cylinders were polished by 50 nm SiO_2 suspension only without grinding, denoted as the 304-Nano samples. It took 1 min of wet grinding for each grade of SiC paper, and the polishing process lasted 10 min.

2.2. Material characterisations

The phase composition of the samples was confirmed by X-ray diffraction (XRD, D8 ADVANCE, Bruker, Germany) with a copper anode at 40 kV and 40 mA scanning at 0.03°/s in a range of 35° to 95°. The calculation of the content of martensite and austenite phase was carried out according to a previous report [22]. Transmission electron microscopy (TEM, Talos F200x, ThemoFisher, USA) was used to characterize the microstructure of the samples. For the TEM characterisation, the specimens were cut from the polished surface of a 304-Nano sample by focused ion beam (FIB, Auriga, Carl Zeiss, Germany). Electron backscattered diffraction (EBSD, e^- FlashHD detector, Bruker, Germany) was carried out at 20 kV and 1 μm step size to characterize the cross-section of the 304 sample. The FIBed 304-Nano sample was also characterized by EBSD using transmission Kikuchi diffraction apparatus at 20 kV and 4 nm step size. For the nano-indentation test, five randomly selected locations on the sample surface were indented by a diamond indenter (Nano Indenter G200, MTS, USA). For the microhardness test (Wilson VH3300, Buehler, Germany), five random sites on the sample surface were indented under a load of 0.1 kgf. The tested samples were also observed by scanning electron microscopy (SEM, Quanta FEG 250, FEI, USA) to analyse the morphology of the indented regions.

The cavitation erosion resistance of the samples was tested in deionized water using ultrasonic vibratory apparatus (GBS-SCT 20 A, Guobiao Ultrasonic Equipment Co., Ltd., Hangzhou, China) as per a modified version of ASTM G32 standard using stationary sample method, and the detailed parameters were described in a previous study [13]. Specifically, the solution temperature was kept at 25 ± 1 °C, the peak-to-peak amplitude of the sonotrode was 50 μm, the gap between the sonotrode tip and sample surface was 1 mm, and the diameter of the

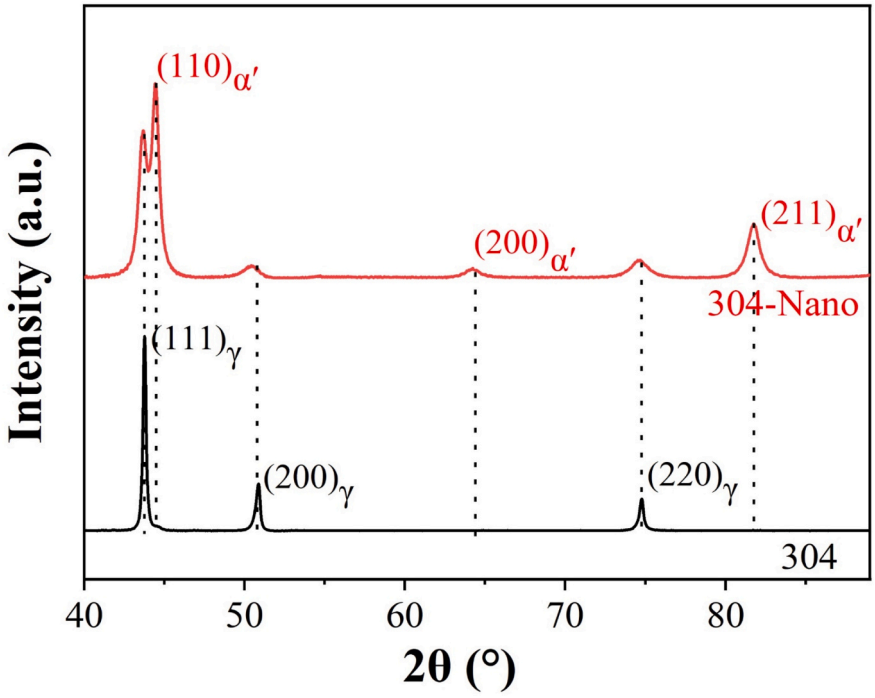

Fig. 1. XRD pattern of the 304 and 304-Nano samples.

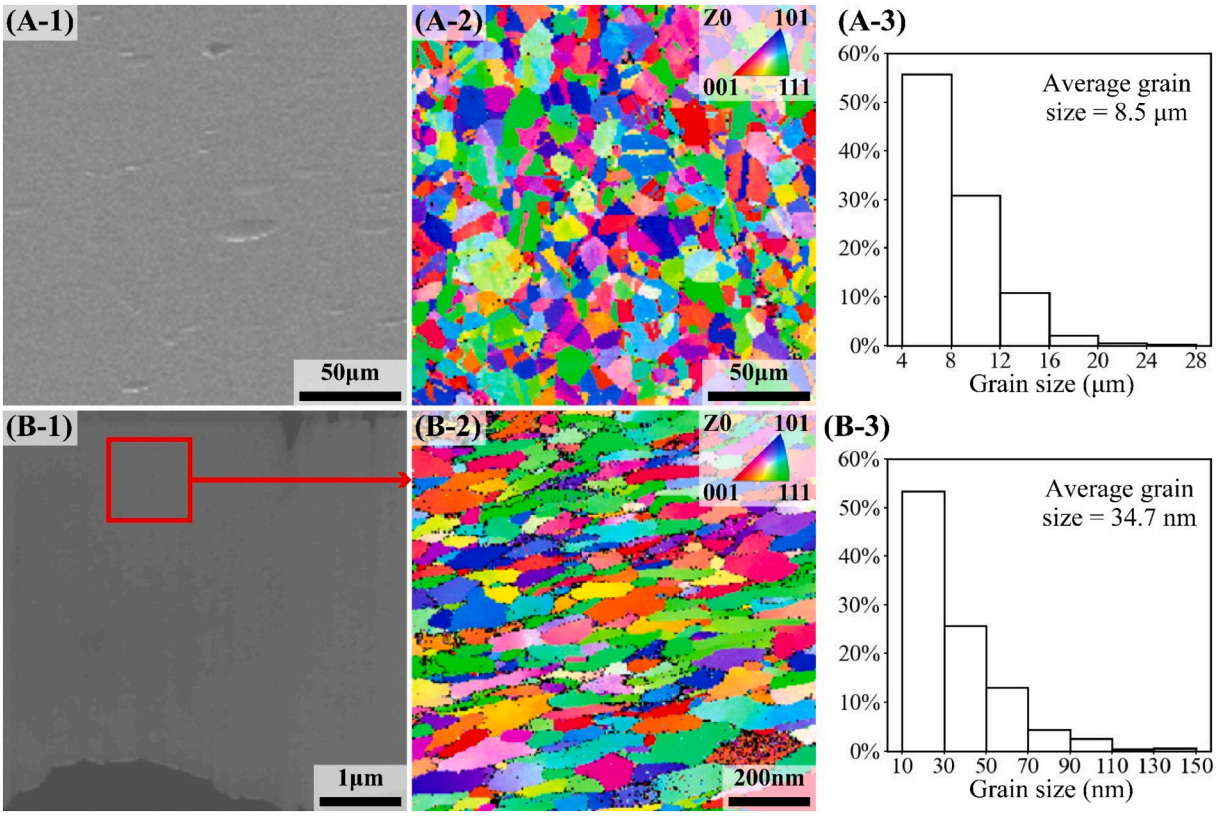

Fig. 2. EBSD mappings for the counting of grain size distribution. A-1 and B-1, SEM images of the mapped regions in the 304 and the 304-Nano samples; A-2 and B-2, invers pole figures showing the grains. A-3 and B-3, grain size distributions.

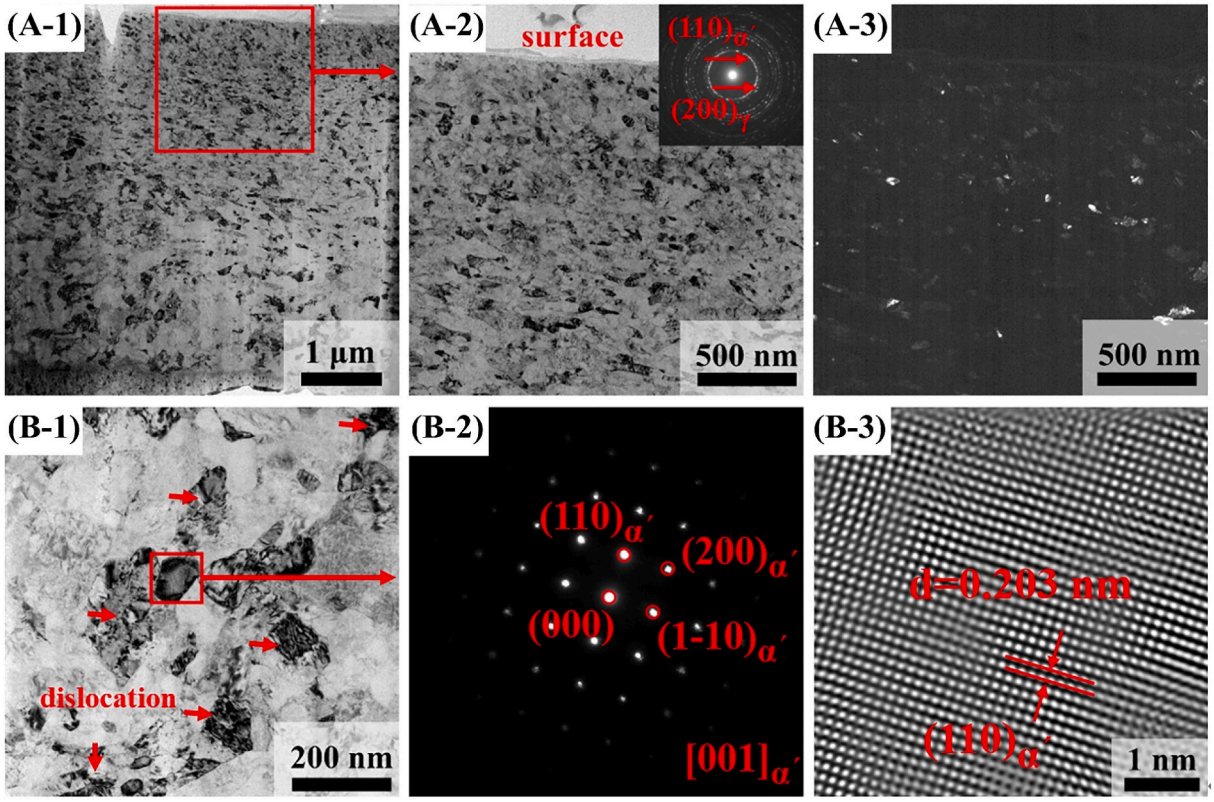

Fig. 3. TEM characterisation of the 304-Nano sample. A-1 and A-2, TEM images of specimen cut by FIB; A-3, the dark field of A-2; B-1, image near the sample surface; B-2, the corresponding selected area electron diffraction (SAED) patterns; B-3, high-resolution TEM image.

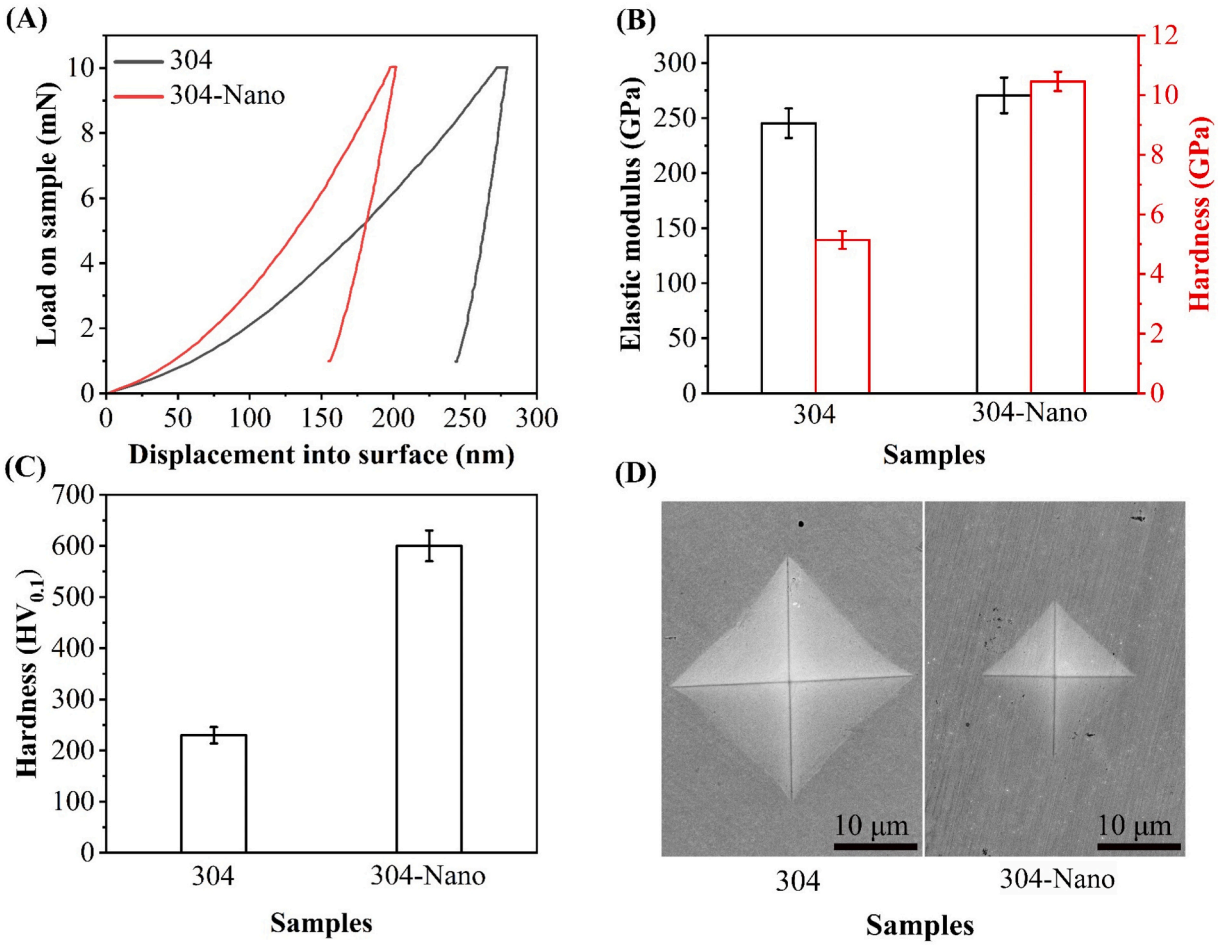

Fig. 4. Mechanical properties of the samples. A, load-displacement plot; B, indentation hardness and indentation modulus; C, Vickers hardness; D, indentation morphology of the 304 and 304-Nano samples after Vickers hardness test.

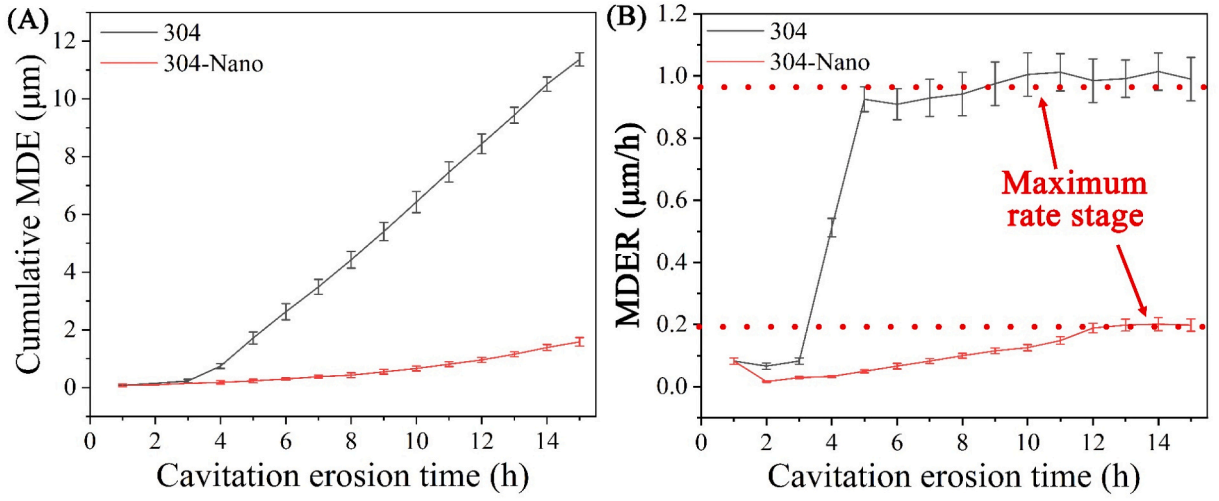

Fig. 5. Cumulative MDE (A) and MDER (B) of the 304 and the 304-Nano samples exposed to cavitation erosion in deionized water for 15 h.

sonotrode tip was 25 mm, which was greater than that of the sample. At each test interval of 1 h, the mass loss of the sample was weighed by an electronic analytical balance (METTLER 220, TOLEDO Instruments Co., Ltd., Shanghai, China). The erosion and the erosion rate were converted to the mean depth of erosion (MDE) and the rate of MDE (MDER) according to ASTM G32 [23], as demonstrated in the equations below, where the V_{loss}, A, m_{loss}, and ρ are the volume loss of the specimen, mass loss of the specimen, area of the specimen exposed to cavitation, and density of the specimen, respectively. The eroded surface of the samples after 15 h of cavitation erosion test were characterized by a 3D profilometer (UP-Lambda, Rtec-Instruments Ltd., USA). Moreover, SEM was also used to investigate the behaviour of the samples exposed to

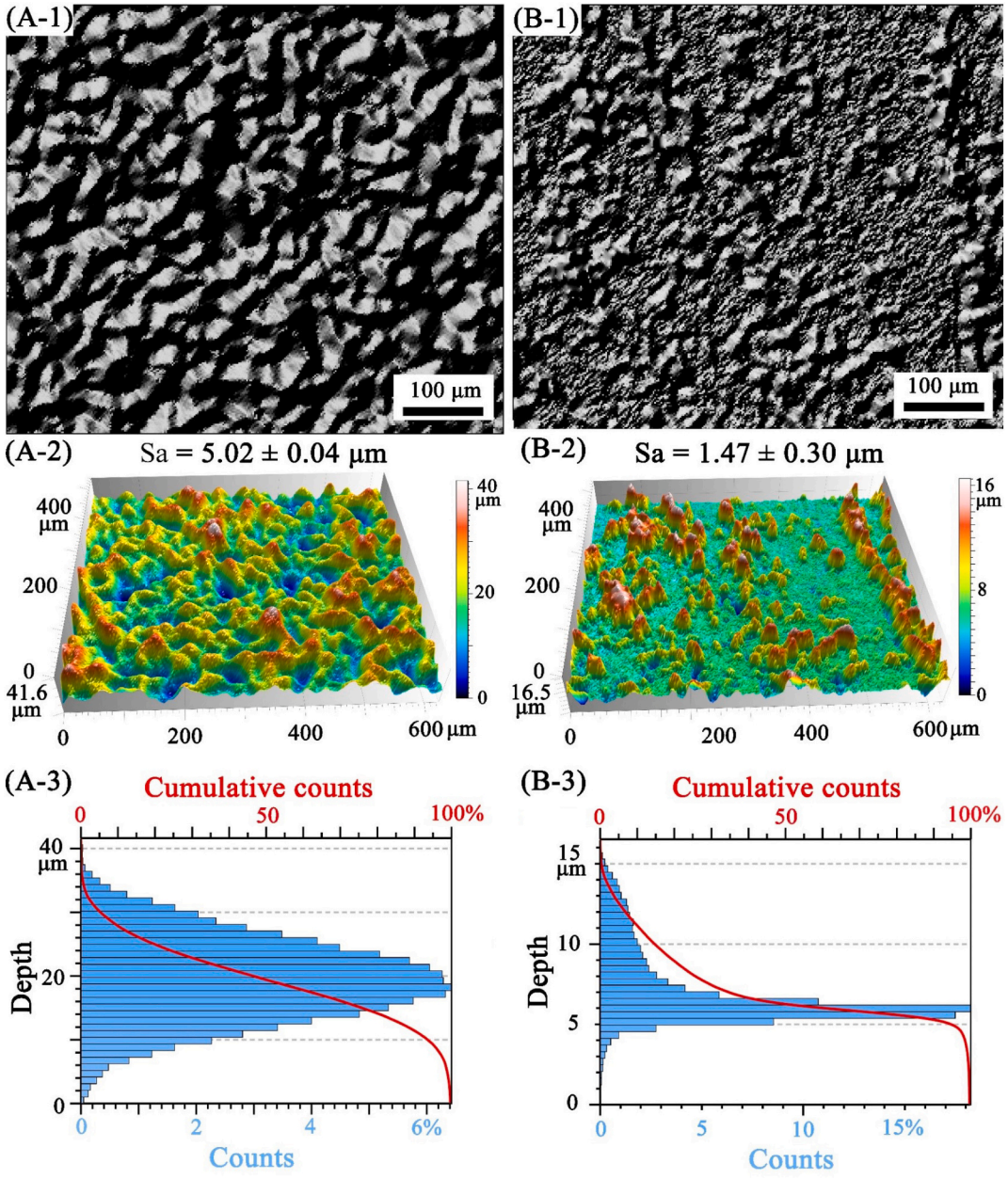

Fig. 6. Optical microscope topography (−1), 3D surfaces topography (−2) and depth distribution on the eroded surface (−3) of the 304 sample (A) and 304-Nano sample (B) after cavitation erosion in deionized water for 15 h.

cavitation erosion.

$$MDE = \frac{V_{loss}}{A} = \frac{m_{loss}}{\rho \bullet A} \quad (1)$$

$$MDER = \frac{\Delta MDE}{\Delta t} \quad (2)$$

3. Results and discussion

Fig. 1 shows the XRD pattern of the 304 and 304-Nano samples. From the XRD results of the 304 sample in Fig. 1, it can be seen that it is a single-phase austenitic stainless steel (γ phase), and the diffraction peaks at 44°, 52° and 75° correspond to (111), (200) and (220) crystals, respectively. The result is consistent with previous reports [24–26]. As for the 304-Nano sample, it not only contains the γ-austenite phase but also contains the α'martensite phase. The presented ά martensite phase was likely formed by the in-situ transformation of γ austenite phase. It is worth noting that the γ(200) and γ(220) diffraction peaks of the 304-Nano sample are significantly shifted to the left compared with those of the original 304 sample, which reflects stress in the austenite phase in the 304-Nano sample. Furthermore, according to the Bragg formula ($2d \cdot \sin\theta = n \cdot \lambda$, $n = 1, 2, 3, \cdots$), when the diffraction angle (θ) is smaller, the interplanar spacing (d) is larger [27], which indicates that there is tensile stress in the austenite phase of the 304-Nano sample. Based on the XRD pattern, the content of the γ-austenite phase and the α' martensite phase in the 304-Nano sample was calculated, and the content of the two phases is 35 % and 65 %, respectively. Generally, there would be a ε phase during the transformation from γ austenite to α' martensite [22,28]. However, no diffraction peaks related to the ε phase were observed in the 304-Nano sample. A similar result was also reported by K.Emurlaev et al. [29]. The authors used synchrotron radiation to investigate the phase transition behaviour of austenitic stainless steel during the friction process. The results showed that the ε phase was only detected at the initial stage of the friction cycle. With the increased

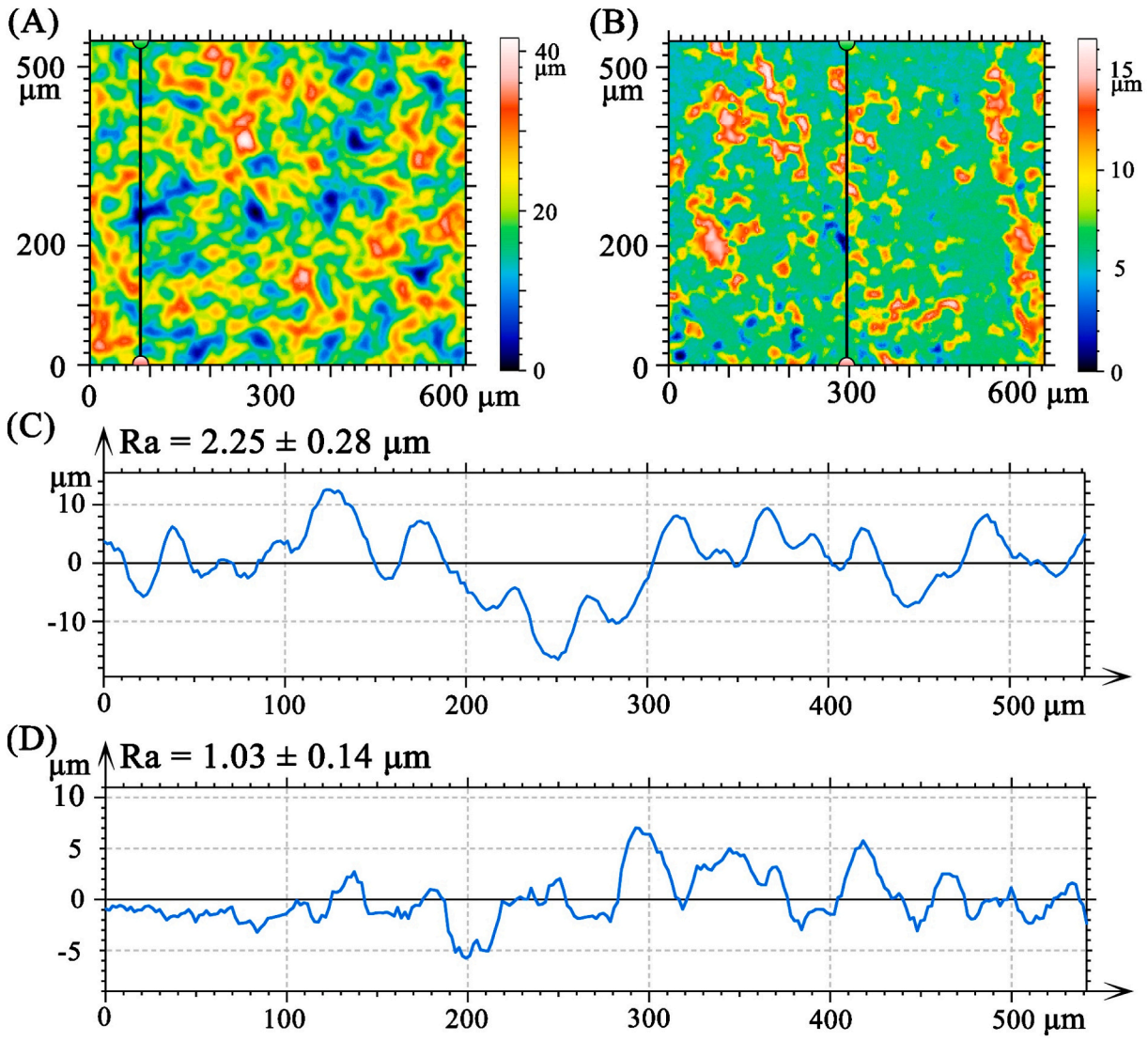

Fig. 7. Surface profiles (A, B) and linear profiles (C, D) of the 304 sample (A, C) and 304-Nano sample (B, D) after cavitation erosion in deionized water for 15 h.

friction cycles, the ε intermediate phase rapidly reduced. When the number of friction cycles increased to 69, the ε phase on the surface of the sample completely disappeared, and the composition of the sample surface was mainly α′martensite phase. Hence, the ε phase was likely to exist during the preparation process of the 304-Nano sample in this study, but due to the repeated friction caused by the high-speed rotation of the saw blade (3800 rpm), the ε phase disappeared rapidly, resulting in no detection of ε phase in the XRD pattern of the 304-Nano sample. Besides, it should be pointed out that the corresponding diffraction peaks can only be detected when the content of the corresponding phase in the sample reaches a mass fraction of more than 3 %, and it is difficult to detect when the mass fraction is below 3 %. Therefore, the absence of ε phase in the XRD of the 304-Nano sample may be also because of its low content.

Fig. 2 shows EBSD mappings of the 304 and 304-Nano samples. The index rate of the 304 sample was 98.7 %. The phase composition of the 304 sample was almost fully austenite with the martensite less than 0.6 %, and the average grain size was 8.5 μm. As for the 304-Nano sample, the index rate was 91.2 %, whose decrease was attributed to the stress accumulation during the mechanical cutting process. The average grain size was significantly refined to 34.7 nm (more than 95 % of the grains were less than 100 nm), and 91.9 % of the mapped region was martensite. According to the calculation based on the previous XRD result, the martensite in the 304-Nano sample was about 65 %, which was lower than the EBSD result. This difference indicates that the affected region by the cutting process was very thin.

Fig. 3 shows the TEM characterisation of the 304-Nano sample. It can be seen that the grain size of the specimen in Fig. 3A-1 becomes smaller as it is closer to the specimen surface. Furthermore, the 304-Nano sample is mainly composed of α′ martensite phase. The selected area diffraction signal of γ austenite phase is not obvious (Fig. 3A-2), only a small amount of γ-austenite was evenly distributed in the sample (Fig. 3A-3). The content of the γ austenite is approximately 8 %, and the content of the α' martensite phase is approximately 92 %, consistent with the EBSD result. Fig. 3B-1 shows many dislocations inside the grains in the sample. According to the corresponding selected area electron diffraction (SAED) pattern, the grains were martensitic nanocrystals (Fig. 3B-2). The interplanar spacing measured by inverse Fourier transform is 0.203 nm (Fig. 3B-3), corresponding to the (110) crystal plane of α'martensite. Thus, based on the TEM results (Fig. 3) and the EBSD result (Fig. 2), a layer of nanocrystals mainly composed of the α' martensitic phase has been successfully constructed on the 304 sample, whose grain size is significantly smaller than that of the original 304 austenitic stainless steel.

Due to the cavitation erosion resistance of the material being determined by its surface mechanical properties, nano-indentation and

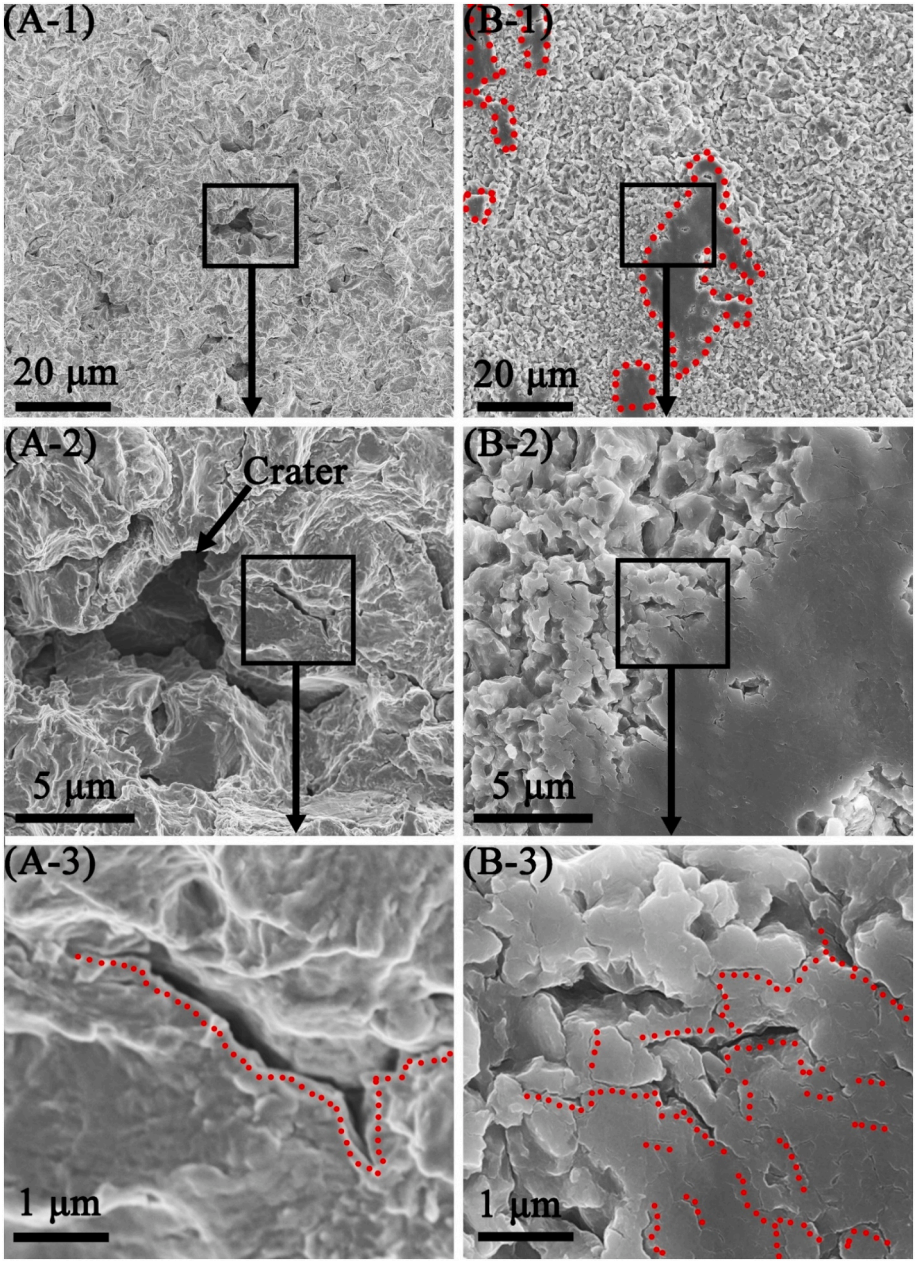

Fig. 8. SEM images showing the surface of the 304 (A) and the 304-Nano sample (B) after cavitation erosion in deionized water for 15 h.

Vickers hardness tests were conducted, and the results are shown in Fig. 4. It can be seen that a larger area is enclosed by the load-displacement curve and the X-axis for the 304 sample, which indicates higher plastic deformation energy absorption (Fig. 4A). Nevertheless, compared with the 304 sample, the nano-indentation hardness and elastic modulus of the 304-Nano sample increased by 106 % and 10.3 %, respectively (Fig. 4B). As for the Vickers hardness (Fig. 4C), the 304 sample showed a value of 230 ± 14 Hv, and the 304-Nano sample exhibited a value of 600 ± 30 Hv. Compared with the 304 sample, the Vickers hardness of the 304-Nano sample increased by 161 %. Similar results were also reported by Selvam et al. [16]. The largest Vickers hardness (420 Hv) of the austenitic stainless steel was obtained by using friction stir welding to refine the surface grains of the material [16], which is significantly smaller than that in this study (600 ± 30 Hv). The Vickers hardness of the 304-Nano sample can be attributed to the following two reasons. First of all, the grain refinement structure prepared by Selvam et al. was mainly composed of austenite [16], while the nanocrystalline layer prepared in this study was mainly composed of martensite (Fig. 1). Generally, the hardness of martensite is greater than that of austenite [30,31]. Secondly, the grain size of the grain-refined structure prepared by Selvam et al. was higher than 600 nm, which is much higher than that in this study (34.7 nm). It is known that the smaller the grain, the harder the material will be [32,33]. Fig. 4D shows the Vickers hardness indentation morphology of the 304 and the 304-Nano samples. There were no cracks around the indentation morphology of the two samples. The results show that although the hardness of the 304-Nano sample was up to 600 ± 30 Hv, it still exhibited good toughness. The microjet and shock wave generated during the cavitation erosion process can inflict heavy impacts on the sample surface. Thus, improving mechanical properties such as hardness will have a positive significance in resisting cavitation erosion.

Fig. 5 shows the cumulative MDE and MDER of the 304 and the 304-Nano samples exposed to cavitation erosion in deionized water for 15 h. After 15 h of cavitation erosion, the cumulative MDE of the 304 samples

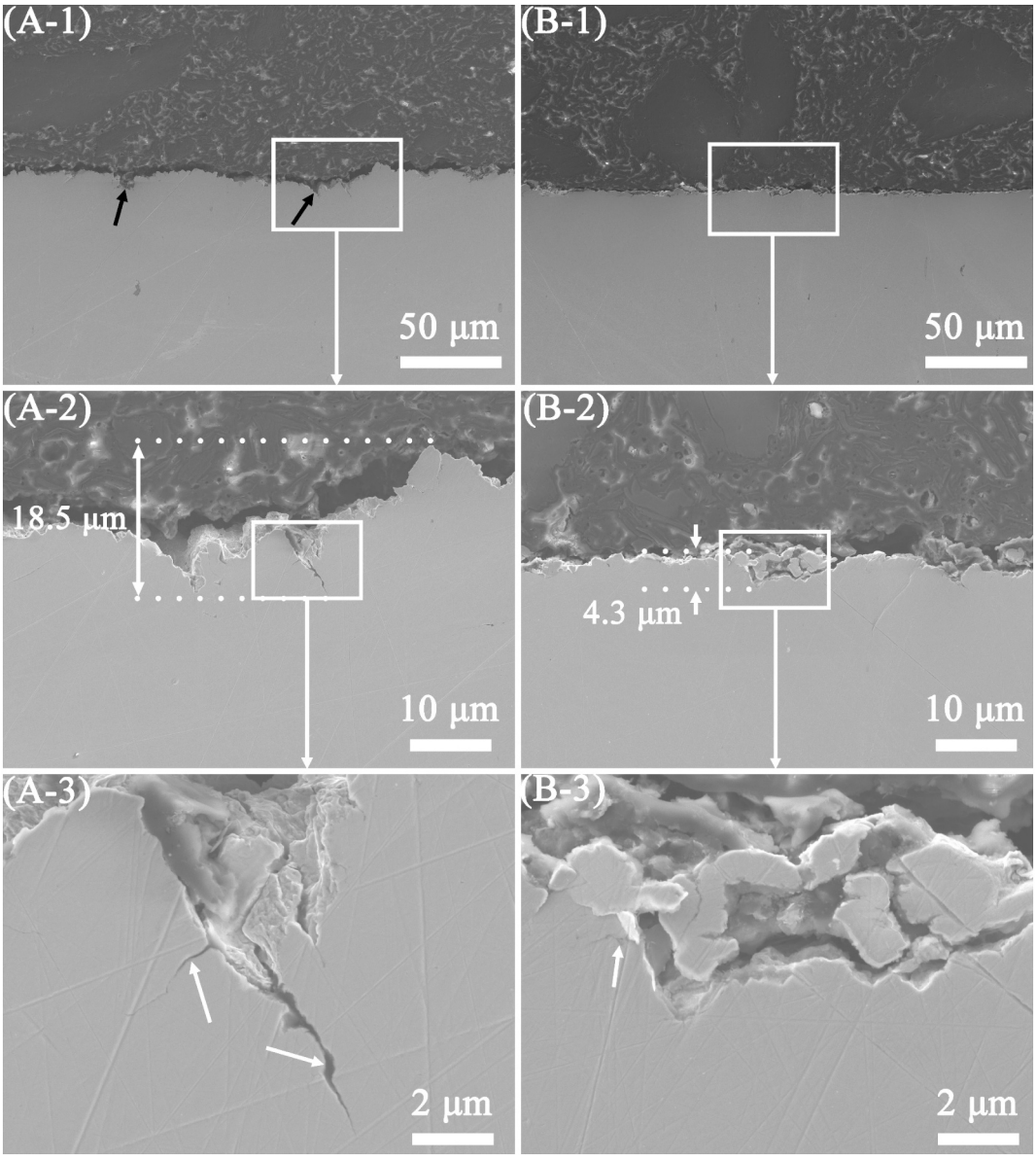

Fig. 9. SEM images showing the cross-section of the 304 (A) and the 304-Nano sample (B) after cavitation erosion in deionized water for 15 h. The black arrows indicate the severely eroded sites.

is 11.37 ± 0.23 μm, while that of the 304-Nano samples is only 1.59 ± 0.15 μm. The cavitation erosion rates of the samples in terms of MDER are plotted in Fig. 5B. The 304 sample reached the stable maximum erosion rate of 0.98 μm/h after the exposure to cavitation for 5 h, while the 304-Nano sample reached the stable maximum erosion rate of 0.19 μm/h at the 12th h. At the maximum erosion rate stage, the erosion rate of the 304-Nano sample was 19.4 % that of the 304 sample, showing that the 304-Nano sample was much more resistant to cavitation erosion than the 304 sample.

The morphological changes of the 304 and 304-Nano samples exposed to cavitation erosion in deionized water for 15 h are presented in Fig. 6. A large number of eroded sites were formed on the surface of the 304 sample after cavitation erosion for 15 h (Fig. 6A-1), while the surface morphology of the eroded 304-Nano sample (Fig. 6B-1) is relatively smoother than that of the 304 sample. Before the exposure to cavitation, both samples exhibited similar surface roughness. The surface roughness (in terms of Sa) of the 304 sample was 12.25 nm, while that of the 304-Nano sample was 9.51 nm (Fig. S1 & Fig. S2). After the exposure to cavitation erosion, their Sa values increased and were very different. The Sa value of the 304-Nano sample after cavitation erosion was 1.47 ± 0.30 μm (Fig. 6B-2), which is only 29.3 % that of the 304 sample (Fig. 6A-2). Generally, a rougher surface after cavitation erosion means more damage during cavitation erosion. The greater surface roughness of the 304 sample indicates that its anti-cavitation erosion performance was worse than that of the 304-Nano sample. In addition, statistics for the depth of the eroded sites are also shown in Fig. 6A-3 and B-3. The result shows that the depth distribution of the eroded sites on the 304 sample after cavitation erosion ranged from 0 to 41.6 μm and nearly fit the normal distribution (Fig. 6A-3). For the 304-Nano sample, the depth distribution after cavitation erosion ranged from 0 to 16.5 μm but did not fit the normal distribution. The results indirectly indicate that the downward growth of the eroded sites on the 304-Nano sample was inhibited, resulting in better cavitation erosion resistance. Fig. 7A-B shows the contour of the 304 and the 304-Nano samples after cavitation erosion. The number and size of the eroded sites on the 304-Nano sample were significantly lower than those of the 304 sample, indicating that the erosion on the 304-Nano sample was significantly lower than the 304 sample. The linear roughness (Ra) of the 304 and the 304-

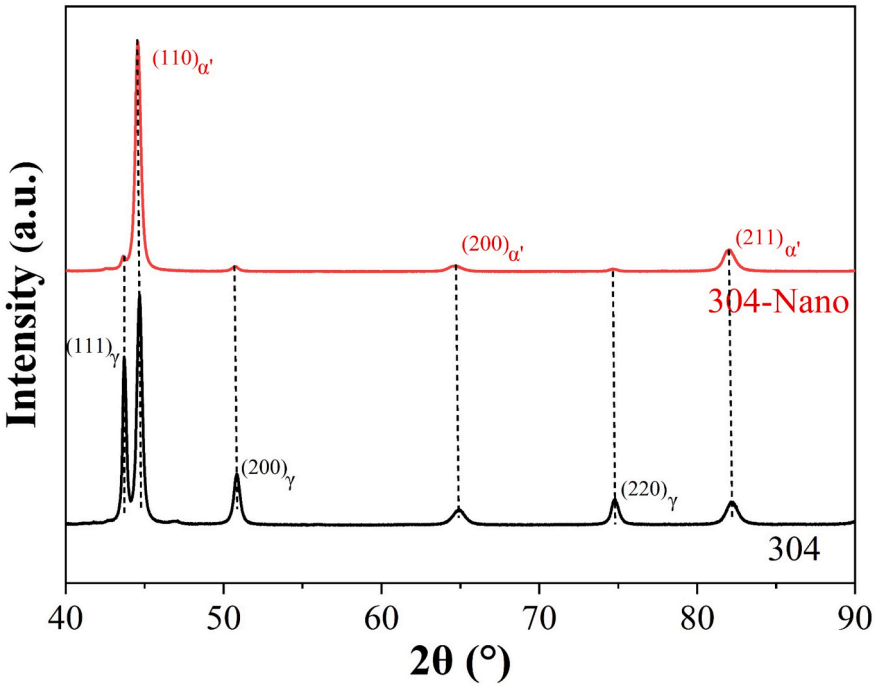

Fig. 10. XRD pattern of the 304 and the 304-Nano samples after 15 h of cavitation erosion.

Nano samples after 15 h cavitation erosion were 2.25 ± 0.28 μm and 1.03 ± 0.14 μm, respectively (Fig. 7C-D). The Ra of the 304 sample was significantly greater than that of the 304-Nano sample, which is consistent with the Sa values (Fig. 6A-2 and B-2). The surface profile results indicate that the ability of the 304-Nano sample to resist the growth of the eroded sites was significantly stronger than that of the 304 sample. These results are consistent with Fig. 5.

Fig. 8 shows the surface morphology of the 304 and the 304-Nano samples after cavitation erosion in deionized water for 15 h. It can be seen that the original morphology of the 304 sample surface (Fig. 8A-1) was completely eroded. As for the 304-Nano sample (Fig. 8B-1), a part of the original surface remained undamaged after cavitation erosion (highlighted by the red dotted boxes). Furthermore, a large eroded site was observed on the surface of the 304 sample (Fig. 8A-2 and A-3), and there is a large crack around the eroded site with a length of approximately 4.5 μm. However, for the 304-Nano sample, it can be seen that more small cracks formed on the surface, but the cracks were dispersed (Fig. 8B-2 and B-3). In general, dispersed and smaller cracks show a greater ability to inhibit crack propagation, resulting in less mass loss and excellent anti-cavitation erosion performance of the 304-Nano sample.

The cross-sections of the 304 and the 304-Nano samples after the exposure to cavitation for 15 h are presented in Fig. 9. At the low magnification (Fig. 9A-1 and B-1), the 304 sample showed a much more jagged surface and larger eroded sites than the 304-Nano sample. The magnified images (Fig. 9A-2 and B-2) show that the eroded site at the 304-Nano sample was much shallower than the eroded site at the 304 sample. According to the further magnified images (Fig. 9A-3 and B-3), microcracks propagated into the 304 sample, while the microcracks in the 304-Nano sample only slightly propagated transversely and could not grow to the deep. Meanwhile, the length of the microcrack in the 304-Nano sample was much shorter than the 304 sample. The results from these cross-sectional SEM images suggest that the 304-Nano sample could inhibit the growth of microcracks but the 304 sample could not, which is in agreement with the results from the SEM images of the surface (Fig. 8).

Fig. 10 presents the XRD pattern of the samples after 15 h of cavitation erosion test. It can be clearly seen from Fig. 9 that austenite and martensite existed in both samples after cavitation erosion. Similar results have been found in other studies [27,34]. The intensity of the austenite peaks ((111)γ, (200)γ, (220)γ) and martensite peaks ((110)α, (200)α), (211)α)) were different, which means the contents of austenite and martensite phases were different in the samples. Further calculation shows that the martensite content of the 304 sample after cavitation erosion was 38 %. Nevertheless, the martensite content of the 304-Nano sample after cavitation erosion increased from 65 % to 94 %, which was significantly higher than the that of the 304 sample. According to the previous study of the 304 stainless steel [35], the content of the transformed martensite reached a maximum before the erosion rate was stabilized. Then, the content would decrease as further exposure to cavitation when the erosion rate became stable. Surprisingly, the 304-Nano sample could preserve the transformed martensite. As a result, the significant difference in the martensite contents of the samples led to a significant difference in the failure mechanism (Fig. 8 and Fig. 9).

Fig. 11 shows the in-situ SEM observation of the cavitation erosion behaviour of the 304 and 304-Nano sample tested in deionized water. Before exposed to cavitation erosion (0 min), the surface of the 304 sample is complete and no cracks are seen (Fig. 11A-1). After 15 min of cavitation erosion, significant deformation was found from the surface of the 304 sample (indicated by the black arrow in Fig. 11A-2). With the extension of the cavitation erosion times (Fig. 11A-2 to A-4), the deformation increased rapidly, showing the accumulation of stress. Meanwhile, deformation twins were observed (Fig. 11A-3). After 90 min of cavitation erosion, the deformations began to evolve into small cavitation pits (highlighted by the red dashed rectangles in Fig. 11A-5). When the cavitation erosion time was 120 min (Fig. 11A-6), the material at the cracks peeled off, forming a cavitation crater with a length of approximately 20 μm. The evolution process of cracks on the surface of the 304 sample into cavitation craters is similar to the previous report [27]. For the 304-Nano sample, the surface was almost intact without any defects such as cracks and pores before cavitation erosion (Fig. 11B-1). After 20 min of cavitation erosion (Fig. 11B-2), cavitation pits (highlighted by the red dashed box) were formed on the sample surface. Some repeated impacts of microjets and shock waves during cavitation erosion were applied on the surface, resulting in the generation of these initial cavitation pits [3]. With the increase of the erosion time to 120

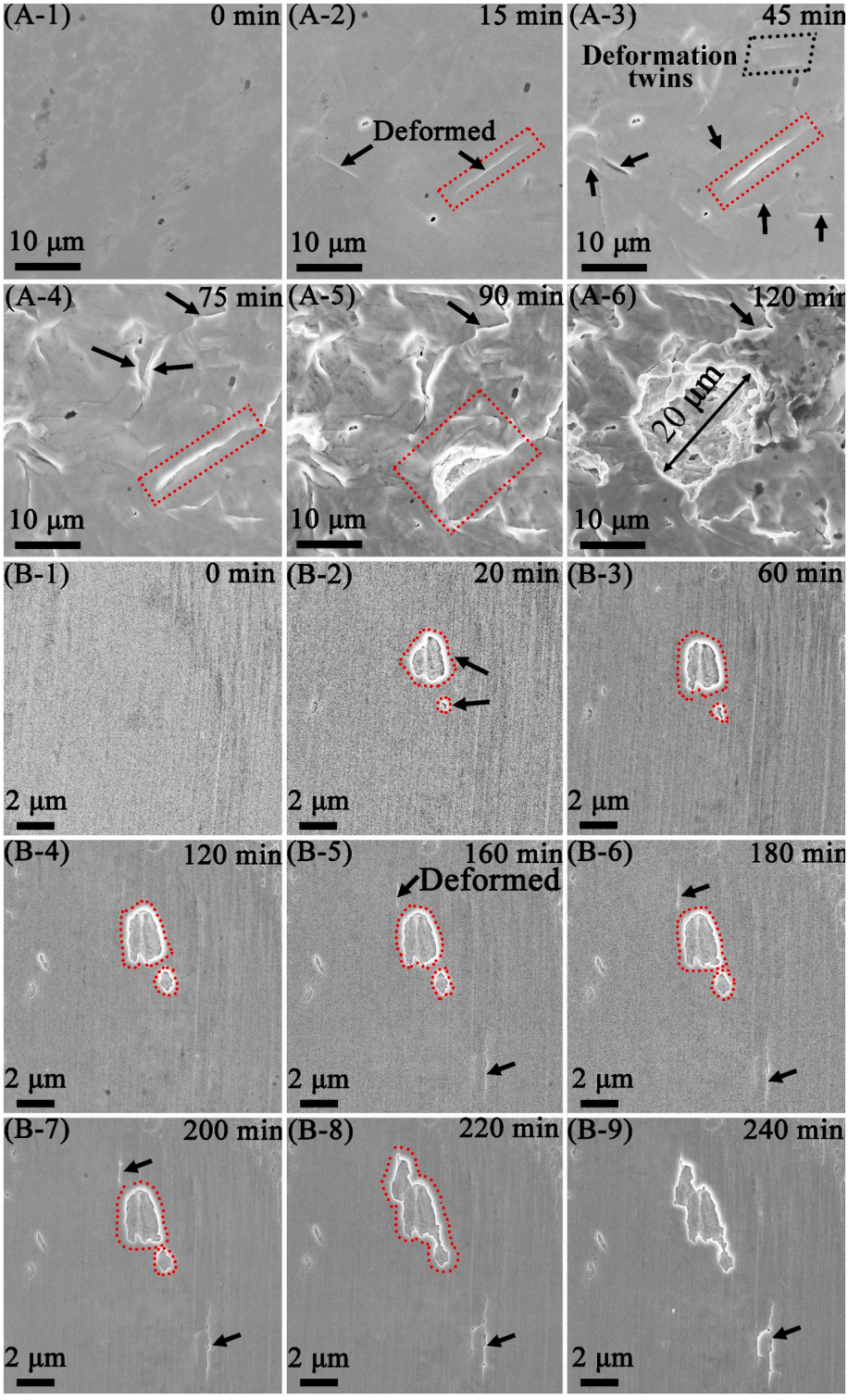

Fig. 11. In-situ observation (at the same observation point) showing the microstructural evolution of the 304 (A) and the 304-Nano sample (B) during cavitation erosion in deionized water.

min (Fig. 11B-2 to B-4), the cavitation pits on the 304-Nano sample surface expanded from 2.4 μm to 2.7 μm. After 160 min of cavitation erosion (Fig. 11B-5), cracks (highlighted by the black arrows) appeared on the surface of the 304-Nano sample. With a further increase of the erosion time to 200 min (Fig. 11B-7), the cavitation pit and cracks further increased and expanded. After 220 min of cavitation erosion (Fig. 11B-8), the cavitation pits integrated together, forming a severely eroded site with a length of approximately 6.2 μm. When eroded for 240 min (Fig. 11B-9), new cracks appeared, and the deformation at the crack (indicated by the black arrow) was more severe, showing more stress accumulation. From the in-situ SEM observation results (Fig. 11), it can be seen that the ability of the 304 sample to inhibit crack initiation and propagation was significantly lower than that of the 304-Nano sample, which was probably attributed to their microstructure. First, the 304 sample is a single-phase fcc austenitic stainless steel, while the 304-Nano sample is mainly composed of bcc martensitic phase. In general, the

hardness of the martensite phase is greater than that of the austenite phase [30,31], and higher hardness is beneficial for resisting cavitation damage [36]. Second, there is a huge difference in grain size between the 304 and the 304-Nano sample. The 304-Nano sample has smaller grains and higher grain boundary density, and the high-density grain boundaries can significantly increase the hardness of the material, resulting in more effective resistance to cavitation erosion [16]. In addition, the high-density grain boundaries are likely to inhibit the expansion of cracks, thereby delaying the formation of cavitation pits. During the initial stage of cavitation erosion process, a large number of dislocations will be generated on the surface of the sample as a response to the cavitation shock wave and microjet. With the further prolongation of the cavitation erosion time, lots of dislocations would slip to the grain boundaries, resulting in the accumulation of grain boundary strain and the generation of cracks [27]. To illustrate the relationship between the force exerted by a single dislocation on the grain boundary and the grain size, critical deformation resistance of grain boundary (τ_{cp}) was introduced [37,38]:

$$\tau_{cp} = D^{*} \ (\Delta\tau)^{2^{*}} \ (2G^{*}b)^{-1} \quad (3)$$

D represents the diameter of the sample grain; G and b represent the elastic modulus and Bragg constants (elastic modulus and Burgers vectors) of the material, respectively; $\Delta\tau$ represents the resolved shear stress of a single dislocation, derived from the input of cavitation microjet and/or shock wave. When assuming the critical deformation resistance (τ_{cp}) of the 304 and 304-Nano sample at the phase boundary is the same, great external input force ($\Delta\tau$) is needed if the grain size (D) is small, indicating the deformation of the phase boundary is more challenging when the grain size (D) is small.

The average grain size of the nanocrystalline layer (the 304-Nano sample) is approximately 34.7 nm, while the grain size of the austenitic stainless steel (the 304 sample) is approximately 8.5 μm. Thus, the external input force ($\Delta\tau$) of the 304-Nano sample is approximately 433 times that of the 304 sample, which means that the grain boundaries of the nanocrystalline layer (the 304 sample) is more difficult to accumulate stress, demonstrating the excellent ability of the nanocrystalline layer to inhibit crack generation and propagation during cavitation erosion. Additionally, it should be noted that the actual development of the dislocation could be much more complex than what was mentioned above [34].

4. Conclusion

Based on the principle of deformation-induced martensitic transformation of austenitic stainless steel, a nanocrystalline layer was successfully prepared on the surface of the 304 austenitic stainless steel via a cutting process. The microstructure, mechanical properties and the cavitation erosion behaviour of the materials were investigated. The following conclusions can be drawn:

1. A nanocrystalline layer mainly composed of α' martensite was formed on the surface of the 304 austenitic stainless steel, and the average grain size of the nanocrystalline layer was 34.67 nm.

2. The Vickers hardness of the nanocrystalline layer on 304 stainless steels (the 304-Nano sample) was much higher than that of the original 304 austenitic stainless steel (the 304 sample).

3. After 15 h of cavitation erosion in deionized water, the erosion rate of the 304-Nano sample was 19.4 % that of the 304 sample, showing the excellent cavitation erosion resistance of the 304-Nano sample.

4. The in-situ SEM observation demonstrated that the 304-Nano sample could effectively inhibit the generation and expansion of cavitation cracks, which was likely attributed to its high-density grain boundaries.

CRediT authorship contribution statement

Nengliang Huang: Writing – original draft, Methodology, Investigation, Formal analysis, Data curation. **Ye Tian:** Writing – review & editing, Methodology, Investigation, Formal analysis. **Rui Yang:** Writing – review & editing, Writing – original draft, Methodology, Formal analysis. **Honghai Ma:** Funding acquisition. **Xiuyong Chen:** Writing – review & editing, Supervision, Funding acquisition, Conceptualization. **Xinkun Suo:** Writing – review & editing, Supervision, Funding acquisition. **Hua Li:** Supervision, Funding acquisition.

Declaration of competing interest

The authors declare that they have no known competing financial interests or personal relationships that could have appeared to influence the work reported in this paper.

Acknowledgement

This research was funded by the Zhejiang Provincial Natural Science Foundation of China (grant # LZ22E090001), and Ningbo 3315 Talents Program (grant # 2020A-29-G).

Appendix A. Supplementary data

Supplementary data to this article can be found online at https://doi.org/10.1016/j.surfcoat.2024.130615.

References

[1] C.E. Brennen, Cavitation bubble collapse, in: C.E. Brennen (Ed.), Cavitation and Bubble Dynamics, Cambridge University Press, Cambridge, 2013, pp. 59–88.
[2] G.L. Chahine, J.-P. Franc, A. Karimi, Cavitation and cavitation Erosion, in: K.-H. Kim, G. Chahine, J.-P. Franc, A. Karimi (Eds.), Advanced Experimental and Numerical Techniques for Cavitation Erosion Prediction, Springer, Netherlands, Dordrecht, 2014, pp. 3–20.
[3] D.H. Edwards, I.R. Jones, An experimental study of the forces generated by the collapse of transient cavities in water, J. Fluid Mech. 7 (1960) 596–609, https://doi.org/10.1017/S0022112060000311.
[4] M.M. Grant, P.A. Lush, Liquid impact on a bilinear elastic-plastic solid and its role in cavitation erosion, J. Fluid Mech. 176 (1987) 237–252, https://doi.org/10.1017/S0022 112087000648.
[5] L. Ye, X. Zhu, Y. He, X. Wei, Ultrasonic cavitation damage characteristics of materials and a prediction model of cavitation impact load based on size effect, Ultrason. Sonochem. 66 (2020) 105115, https://doi.org/10.1016/j.ultsonch.2020.105115.
[6] X. Liu, Y. Luo, Z. Wang, A review on fatigue damage mechanism in hydro turbines, Renew. Sust. Energ. Rev. 54 (2016) 1–14, https://doi.org/10.1016/j.rser.2015.09.025.
[7] B.K. Sreedhar, S.K. Albert, A.B. Pandit, Cavitation damage: theory and measurements – a review, Wear 372-373 (2017) 177–196, https://doi.org/10.1016/j.wear.2016.12.009.
[8] R. Bensow, The numerical prediction of cavitation and related nuisance in marine propulsion systems, in: M.G. Phoevos Koukouvinis (Ed.), Cavitation and Bubble Dynamics: Fundamentals and Applications, Academic Press, 2021, pp. 111–132.
[9] S. Hong, Y. Wu, J. Zhang, Y. Zheng, Y. Qin, J. Lin, Ultrasonic cavitation erosion of high-velocity oxygen-fuel (HVOF) sprayed near-nanostructured WC-10Co-4Cr coating in NaCl solution, Ultrason. Sonochem. 26 (2015) 87–92, https://doi.org/10.1016/j.ultsonch.2015.01.012.
[10] L. Qiao, Y. Wu, S. Hong, J. Cheng, Ultrasonic cavitation erosion mechanism and mathematical model of HVOF sprayed Fe-based amorphous/nanocrystalline coatings, Ultrason. Sonochem. 52 (2019) 142–149, https://doi.org/10.1016/j.ultsonch.2018.11.010.
[11] Z.B. Zheng, Y.G. Zheng, W.H. Sun, J.Q. Wang, Effect of heat treatment on the structure, cavitation erosion and erosion–corrosion behavior of Fe-based amorphous coatings, Tribol. Int. 90 (2015) 393–403, https://doi.org/10.1016/j.triboint.2015.04.039.
[12] L. Qiao, Y. Wu, S. Hong, J. Zhang, W. Shi, Y. Zheng, Relationships between spray parameters, microstructures and ultrasonic cavitation erosion behavior of HVOF sprayed Fe-based amorphous/nanocrystalline coatings, Ultrason. Sonochem. 39 (2017) 39–46, https://doi.org/10.1016/j.ultsonch.2017.04.011.
[13] Y. Tian, R. Yang, Z. Gu, H. Zhao, X. Wu, S.T. Dehaghani, H. Chen, X. Liu, T. Xiao, A. McDonald, H. Li, X. Chen, Ultrahigh cavitation erosion resistant metal-matrix composites with biomimetic hierarchical structure, Compos. Part B-Eng. 234 (2022) 109730, https://doi.org/10.1016/j.compositesb.2022.109730.
[14] R. Yang, N. Huang, Y. Tian, J. Qin, P. Lu, H. Chen, H. Li, X. Chen, Insights into the exceptional cavitation erosion resistance of laser surface melted Ni-WC compo-

sites: the effects of WC morphology and distribution, Surf. Coat. Technol. 444 (2022) 128685, https://doi.org/10.1016/j.surfcoat.2022.128685.
[15] M. Nowakowska, L. Łatka, P. Sokołowski, M. Szala, F.-L. Toma, M. Walczak, Investigation into microstructure and mechanical properties effects on sliding wear and cavitation erosion of Al_2O_3-TiO_2 coatings sprayed by APS, SPS and S-HVOF. Wear 508-509 (2022) 204462, https://doi.org/10.1016/j.wear.2022.204462.
[16] K. Selvam, P. Mandal, H.S. Grewal, H.S. Arora, Ultrasonic cavitation erosion-corrosion behavior of friction stir processed stainless steel, Ultrason. Sonochem. 44 (2018) 331–339, https://doi.org/10.1016/j.ultsonch.2018.02.041.
[17] J.D. Escobar, E. Velásquez, T.F.A. Santos, A.J. Ramirez, D. López, Improvement of cavitation erosion resistance of a duplex stainless steel through friction stir processing (FSP), Wear 297 (2013) 998–1005, https://doi.org/10.1016/j.wear.2012.10.005.
[18] Y. Li, Y. Lian, Y. Sun, Cavitation erosion behavior of friction stir processed nickel aluminum bronze, J. Alloys Compd. 795 (2019) 233–240, https://doi.org/10.1016/j.jallcom.2019.04.302.
[19] Y. Li, Y. Lian, Y. Sun, Comparison of cavitation erosion behaviors between the as-cast and friction stir processed Ni-Al bronze in distilled water and artificial seawater, J. Mater. Res. Technol. 13 (2021) 906–918, https://doi.org/10.1016/j.jmrt.2021.05.015.
[20] L. Zhu, H. Ruan, A. Chen, X. Guo, J. Lu, Microstructures-based constitutive analysis for mechanical properties of gradient-nanostructured 304 stainless steels, Acta Mater. 128 (2017) 375–390, https://doi.org/10.1016/j.actamat.2017.02.035.
[21] H.W. Zhang, Z.K. Hei, G. Liu, J. Lu, K. Lu, Formation of nanostructured surface layer on AISI 304 stainless steel by means of surface mechanical attrition treatment, Acta Mater. 51 (2003) 1871–1881, https://doi.org/10.1016/s1359-6454(02)00594-3.
[22] A.K. De, D.C. Murdock, M.C. Mataya, J.G. Speer, D.K. Matlock, Quantitative measurement of deformation-induced martensite in 304 stainless steel by X-ray diffraction, Scr. Mater. 50 (2004) 1445–1449, https://doi.org/10.1016/j.scriptamat.2004.03.011.
[23] ASTM, ASTM-G32, Standard Test Method for Cavitation Erosion Using Vibratory Apparatus, West Conshohocken, PA, 2010.
[24] D. Kaoumi, J. Liu, Deformation induced martensitic transformation in 304 austenitic stainless steel: in-situ vs. ex-situ transmission electron microscopy characterization, Mater. Sci. Eng. A 715 (2018) 73–82, https://doi.org/10.1016/j.msea.2017.12.036.
[25] E.A. Eid, M.M. Sadawy, A.M. Reda, Computing the dynamic friction coefficient and evaluation of radiation shielding performance for AISI 304 stainless steel, Mater. Chem. Phys. 277 (2022) 125446, https://doi.org/10.1016/j.matchemphys.2021.125446.
[26] Y.F. Shen, X.X. Li, X. Sun, Y.D. Wang, L. Zuo, Twinning and martensite in a 304 austenitic stainless steel, Mater. Sci. Eng. A 552 (2012) 514–522, https://doi.org/10.1016/j.msea.2012.05.080.
[27] Y. Tian, H. Zhao, R. Yang, X. Liu, X. Chen, J. Qin, A. McDonald, H. Li, In-situ SEM investigation on stress-induced microstructure evolution of austenitic stainless steels subjected to cavitation erosion and cavitation erosion-corrosion, Mater. Design 213 (2022) 110314, https://doi.org/10.1016/j.matdes.2021.110314.
[28] A.Y. Chen, H.H. Ruan, J. Wang, H.L. Chan, Q. Wang, Q. Li, J. Lu, The influence of strain rate on the microstructure transition of 304 stainless steel, Acta Mater. 59 (2011) 3697–3709, https://doi.org/10.1016/j.actamat.2011.03.005.
[29] K. Emurlaev, I. Bataev, I. Ivanov, D. Lazurenko, V. Burov, A. Ruktuev, D. Ivanov, M. Rosenthal, M. Burghammer, K. Georgarakis, A.M. Jorge Junior, Friction-induced phase transformations and evolution of microstructure of austenitic stainless steel observed by operando synchrotron X-ray diffraction, Acta Mater. 234 (2022) 118033, https://doi.org/10.1016/j.actamat.2022.118033.
[30] J. Mola, M. Ren, On the hardness of high carbon ferrous martensite, IOP Conf. Ser.: Mater. Sci. Eng. 373 (2018) 012004, https://doi.org/10.1088/1757-899X/373/1/012004.
[31] J.R.C. Guimarães, C. Rios Maria, The hardness of martensite-austenite mixtures in Fe-31.9% Ni-0.02% C, Mater. Sci. Eng. 43 (1980) 55–58, https://doi.org/10.1016/0025-5416(80)90207-4.
[32] H. Yin, M. Song, P. Deng, L. Li, B.C. Prorok, X. Lou, Thermal stability and microstructural evolution of additively manufactured 316L stainless steel by laser powder bed fusion at 500–800 °C, Addit. Manuf. 41 (2021) 101981, https://doi.org/10.1016/j.addma.2021.101981.
[33] Y. Mai, X. Jie, L. Liu, N. Yu, X. Zheng, Thermal stability of nanocrystalline layers fabricated by surface nanocrystallization, Appl. Surf. Sci. 256 (2010) 1972–1975, https://doi.org/10.1016/j.apsusc.2009.09.030.
[34] A. Krella, Influence of cavitation intensity on X6CrNiTi18-10 stainless steel performance in the incubation period, Wear 258 (2005) 1723–1731, https://doi.org/10.1016/j.wear.2004.11.025.
[35] L.M. Zhang, Z.X. Li, J.X. Hu, A.L. Ma, S. Zhang, E.F. Daniel, A.J. Umoh, H.X. Hu, Y. G. Zheng, Understanding the roles of deformation-induced martensite of 304 stainless steel in different stages of cavitation erosion, Tribol. Int. 155 (2021) 106752, https://doi.org/10.1016/j.triboint.2020.106752.
[36] Z. Liu, A. Khan, M. Shen, S. Zhu, C. Zeng, F. Wang, C. Fu, Microstructure and cavitation erosion resistance of arc ion plating NiCrAlY coating on the 304L stainless steel, Tribol. Int. 173 (2022) 107618, https://doi.org/10.1016/j.triboint.2022.107618.
[37] Y. Tian, H. Zhao, R. Yang, H. Zhang, M. Yu, P. Zhou, H. Li, X. Chen, Behavior of the hard phases of copper alloys subjected to cavitation erosion investigated by SEM observation, Tribol. Int. 174 (2022) 107771, https://doi.org/10.1016/j.triboint.2022.107771.
[38] L.M. Zhang, A.L. Ma, H. Yu, A.J. Umoh, Y.G. Zheng, Correlation of micro- structure with cavitation erosion behaviour of a nickel-aluminum bronze in simulated seawater, Tribol. Int. 136 (2019) 250–258, https://doi.org/10.1016/j.triboint.2019.03.071.